PhotoniX

RESEARCH Open Access

Metasurface enabled broadband, high numerical aperture Laplace differentiator under multiple polarization illumination

Chen Zhou[1,2], Naseer Muhammad[1,2], Ruizhe Zhao[1,2], Yanjie Chen[1,2], Guangzhou Geng[3], Junjie Li[3], Xiaowei Li[4], Xin Li[1,2*], Yongtian Wang[1,2*] and Lingling Huang[1,2*]

*Correspondence: lix@bit.edu.cn; wyt@bit.edu.cn; huanglingling@bit.edu.cn

[1] Beijing Engineering Research Center of Mixed Reality and Advanced Display, MIIT Key Laboratory of Photonics Information Technology, School of Optics and Photonics, Beijing Institute of Technology, Beijing 100081, China
[2] National Key Laboratory on near-Surface Detection, Beijing 100072, China
[3] Beijing National Laboratory for Condensed Matter Physics, Institute of Physics, Chinese Academy of Sciences, Beijing 100191, China
[4] Laser Micro/Nano-Fabrication Laboratory, School of Mechanical Engineering, Beijing Institute of Technology, Beijing 100081, China

Abstract

Optical metasurfaces to perform optical analog spatial differentiation operations and image edge detection processing is a currently hot topic. However, some metasurface differentiators are limited by polarization dependence, narrow operating bandwidth, low numerical aperture (NA), requiring for additional polarization elements or digital processing, and under coherent light illumination conditions. Here, we use the optical angular dispersion effect based on resonant dielectric metasurface, to realize the Laplacian differential operation in the real space directly, which can address these critical metrics for p- and s-polarized light. Moreover, the broadband operating range of the metasurface differentiator can be obtained by exciting and detuning the electric toroidal dipole (ETD) and magnetic toroidal dipole (MTD) resonances. We experimentally demonstrate that azimuthal-insensitive Laplace differential operations and dual-polarization second-order two-dimensional edge detection with NA up to 0.64 and spectral bandwidths of nearly 100 nm from 750 to 850 nm. In addition, broadband incoherent and unpolarized edge detection experiments are also carried out with satisfactory performance. Our work will pave the way for free-space realization of high-efficiency, broadband parallel optical-computation and image-processing in machine-vision, biomedical, and optical microscopy.

Keywords: Metasurface, Laplace differentiator, Edge detection, Toroidal dipole resonance

Introduction

The image processing in realistic scenarios plays a key role in augmented and virtual reality (AR/VR) in meta-universe, biomedical imaging, autonomous driving and machine vision [1–4]. Currently, the image processing technology mainly relies on digital image processing treatments which is limited by slow operation speed, large physical size, high energy consumption and cost. Therefore, optical computing methods leveraging relevant optical effects such as resonance or the spin Hall effect, which enable image processing technologies to perform massively parallel operations at light-speed with low energy consumption and robustness are useful alternative [5–10]. While conventional

optical elements such as glass lenses suffer from large footprints and integration difficulties. The micro- and nanodevices that can maintain compactness and functional versatility has been proposed to solve these problems [11, 12]. In particular, meta-devices represented by metasurface have been applied to achieve optical analog computation and image processing [13–15]. Especially, optical analog differential operations and image edge detection have been achieved with considerable theoretical and technological breakthroughs[16–22].

The classical Fourier filtering method can realize optical analog differential operations and image edge detection [23]. Wherein, a 4f lens system is used to complete the Fourier transform and inverse transform on the input image, and specific optical filters or spatially-selective masks are embedded to deal with different information frequency components. Although, this approach is easy to understand, the large volume is not suitable for high degree of integration applications. Meanwhile, the easy misalignment between the components would directly affect the image edge detection processing results of the whole integrated system. Recently, using the Green's function method, the angle-dependent optical response can be designed by using metasurface in real space to avoid the Fourier transform process, which can yield more compact and robust image edge detection results [24–31]. However, most of these methods rely on independent and singular resonant modes excited by the differentiator, which not only results in a limited numerical aperture (NA) for analog differential operation and with polarization dependence, but also leads to unidirectional differential results that cannot be processed in two dimensions in a single shot. Additionally, most of these approaches are operating in a narrow bandwidth and require coherent optical illumination. These problems hinder such differential devices in applications particularly, in autonomous driving. So, an all-optical two-dimensional image processing device with large NA and broadband working spectrum that can work under coherent and incoherent illumination conditions is highly desired.

To realize the desired metasurface differentiators it is necessary to choose suitable working principle and ensure compatibility with manufacturing feasibility. For the aim to achieve broadband response of the metasurface, one can either design Pancharatnam-Berry phase metasurface or optical resonant metasurface [20, 32–34]. However, the former generally needs to be accompanied with extra polarizers, which limits the integration effect. In the latter case, most resonant metasurface often has low numerical aperture, which in consequence affects the spatial resolution for edge detection. Meanwhile, there is often trade-off between broadband response, transmittance intensity and high resolution. Besides, it is not easy to obtain polarization multiplexing, even resonant metasurface with C_2 or C_4 rotational symmetry essentially exhibit a polarization asymmetric response at large incidence angle. Therefore, it is helpful to use periodic structures with C_6 rotational symmetry to guarantee azimuthal independence at oblique incidence angles [35, 36]. Furthermore, the vast majority of current analog optical computational methods for image edge detection using metasurface require spatial coherence of the incident light. Even though there are research works that propose the use of double-layer grating structures, multilayer film structures, or nested circular structures to accomplish edge detection using incoherent light sources, the cost is aided by digitized post-processing or 4f systems [37–39].

In this work, a metasurface composed of dielectric cylinders with hexagonal lattice period is demonstrated experimentally to realize second-order two-dimensional (2D) image edge detection directly in the real space. Our metasurface differentiator operates in transmission mode, which is advantageous for direct integration with commercially available optical imaging or sensing systems. The second-order 2D edge detection performances are tested under p-, s-, and unpolarized light in 750—850 nm waveband. The highest numerical aperture and resolution in this work are 0.64 and ~ 0.76 μm, respectively. Such metasurface may provide a new platform for optical computation, advanced microscopic imaging systems and machine vision, etc.

Description of the physical mechanism of differentiation

According to the Fourier optics principle, any image can be decomposed into a series of angular spectrum f_{in} determined by different incidence angles θ, azimuth φ, and the angular spectrum of the corresponding amplitude $E_{in}(x, y)$ according to the Fourier transform are: $f_{in} = \int e^{-i(k_x x + k_y y)} E_{in}(x, y) dxdy$, where $k_x = k_0 \sin\theta \cos\varphi$ and $k_y = k_0 \sin\theta \sin\varphi$ denote the components of the wave vector along the two orthogonal axes x and y, respectively, and $k_0 = 2\pi / \lambda$. In a standard imaging system setup, these angular spectra are re-collected and refocused by a lens. Then, the original image can be reconstructed by performing the corresponding Fourier inverse transform. Thus, along the direction of light propagation, the goal of various mathematical operations such as differentiation defined in Fourier space can be achieved by selectively filtering the component plane waves from the image. Compared to natural materials, it is significantly easier to obtain angular selective filtering operations with metasurface. As it is necessary to encode the desired mathematical operations in the optical transfer function (OTF) of the metasurface.

In order to capture information about all the profiles of an image, the simplest method is to obtain the Laplace differential operator $E_{out}(x, y) = (\partial^2/\partial x^2 + \partial^2/\partial y^2) E_{in}(x, y)$, that can perform second-order 2D edge detection. It is equivalent to a high-pass filter in Fourier space and can be expressed as $f_{out}(k_x, k_y) = -(k_x^2, k_y^2) f_{in}(k_x, k_y)$ in the Fourier domain. In other words, such a metasurface differentiator needs to prevent low frequency components while ensure the successful transmission of high frequency components. As shown in Fig. 1, when the input light passes through the metasurface, the light field information will be directly processed at the speed of light, and the output light field is the result of the Laplace differentiation operation.

However, in order to perform the Laplace differentiation operation for the input image in both p- and s-polarized channels in the same wavelength range, the differentiator should be independent of all azimuthal variations over a large angular range in both polarization channels. The optical transfer function of the designed metasurface should satisfy the following form [40]:

$$t(k_x, k_y) = \begin{bmatrix} t_{ss}(k_x, k_y) & t_{sp}(k_x, k_y) \\ t_{ps}(k_x, k_y) & t_{pp}(k_x, k_y) \end{bmatrix} = \begin{bmatrix} c_{ss} & 0 \\ 0 & c_{pp} \end{bmatrix} k_{||} \tag{1}$$

where the subscripts s and p denote the polarization of the incident and transmitted beams, respectively, $k_{||}^2 = k_x^2 + k_y^2$ denotes the in-plane wave vector. Therefore, the optical transfer function of the designed metasurface should satisfy a quadratic relationship

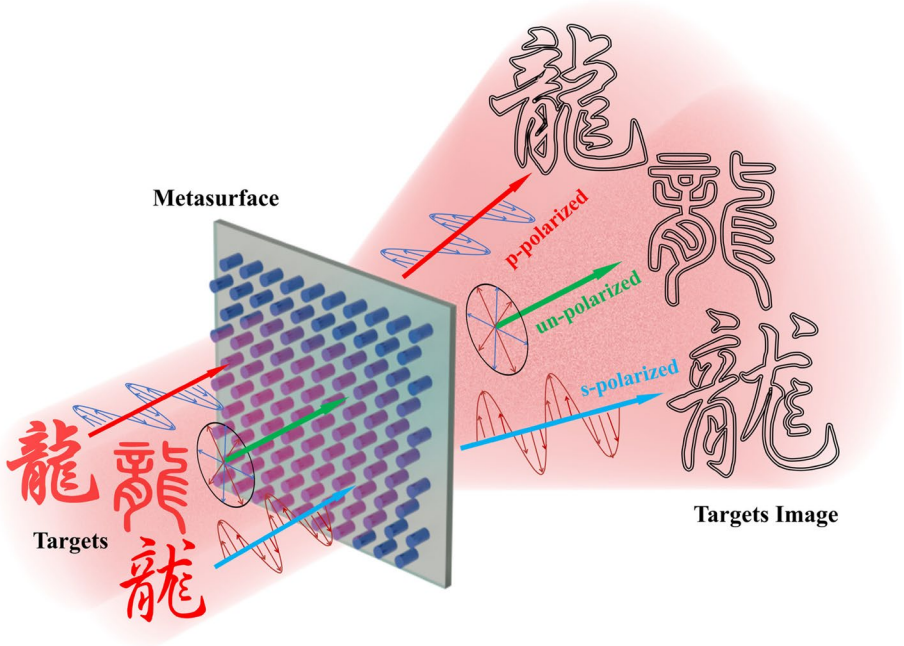

Fig.1 Broadband, high numerical aperture Laplace differentiator under multiple polarization illumination. Schematic illustration of three different forms of the Chinese character "Long" subjected to Laplace differential operation through the cylindrical resonant metasurface under s-polarized, p-polarized, and unpolarized illumination conditions, respectively

with the plane wave vector of the incident. In physical perspective this corresponds to the fact that the transmittance is zero for normal incidence, whereas the transmittance should satisfy the quadratic relationship for oblique incidence.

In practice, to guarantee the second order 2D edge detection obtained from the image after performing the Laplace differentiation operation, it is necessary to adjust the relevant parameters of the metasurface and balance the key metrics. For example, to be able to process high-resolution images without distortion, it is required that the numerical aperture of the metasurface satisfies $NA = n\sin(\theta_{\max}) \geq nk_{in,\max}/k_0$, where, n is the refractive index of air, generally taken as 1, $\theta_{\max}$ represents the maximum incident angle in the input light waves, and $k_{in,\max}$ represents the maximum wave vector in the Fourier decomposition of the input image. Consequently, in order to achieve an effective operational state as described in Eq. (1), it needs to be maintained within a sufficiently large incident angle. In addition, the values of c_{ss} and c_{pp} affect the intensity of the image after differential processing in edge detection. Furthermore, the response from Eq. (1) is generally easy to obtain for certain wavelengths, but in order to cope with the various objective conditions, the broadband operation is preferred. It is of great significance to design a metasurface differentiator with broadband response, multiple polarization channels, and high resolution.

Results

Design of metasurface

Based on the above analysis, the aim of this work is to design a second-order 2D edge-detecting metasurface Laplace differentiator to achieve the above goals. Firstly, it is inspired by the fact that the coupling effect between two resonant modes can be induced to produce a broadband of high transmittance or reflectance [41]. Therefore, it is possible to design two resonant modes with different frequencies in the resonant metasurface by the variation of the geometrical parameters to induce a broad spectral feature with zero or near zero transmittance under normal incidence. This method can provide the prerequisites for a large range of operating bandwidths, compared to the counterpart with one low Q-factor resonant mode. Next, it is required that these two modes sustain the resonance wavelengths or observe small shift as the angle of incidence increases. Meanwhile, it also allows the structure to maintain the quadratic relationship of intensity and wave vector in both p- and s-polarization cases. Thus, these can provide the basis for realizing the optical transfer function of the Laplace differential operator for dual-polarization channels, large NA, high-resolution, and broadband incoherent optical Laplacian differential operators.

According to the above analysis, a single-layer silicon cylindrical metasurface differentiator with hexagonal lattice period placed on a glass substrate is designed, as shown in Fig. 2a. Its performance is mainly determined by three parameters, namely, the lattice constant P, the height H, and the radius R. In order to achieve an operating wavelength near 800 nm, the lattice constant is fixed to P = 420 nm, and the height and radius of

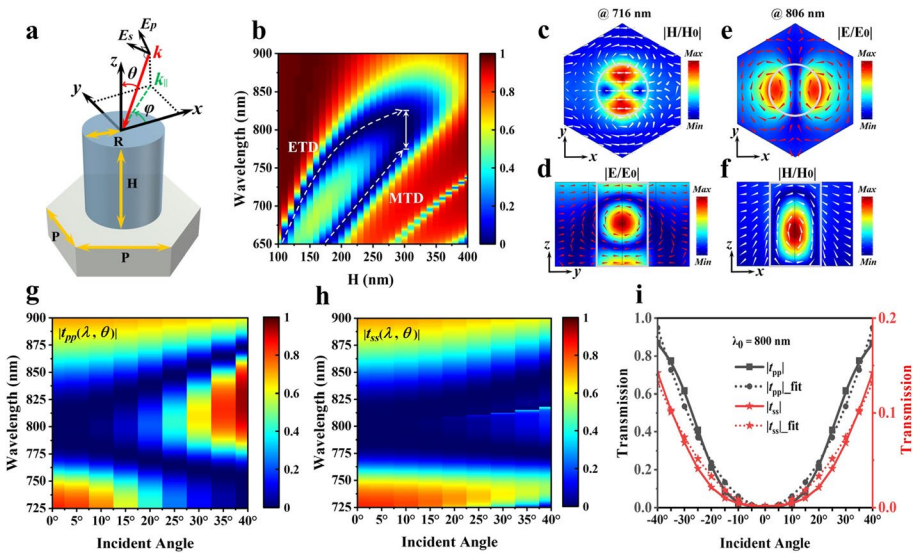

Fig. 2 The geometry design and transmission property of the cylindrical resonant metasurface. **a** Schematic of the metasurface and incident source, where θ and φ are the incidence and azimuthal angle, respectively. **b** Transmission spectra by sweeping the height H, with lattice period P = 420 nm and radius R = 90 nm under p-polarized incidence. **c**-**d** and **e**–**f** Normalized electric and magnetic field profiles in the x–y, y–z and x–z planes at the resonance wavelength of 716 nm and 806 nm when P = 420 nm, R = 90 nm, and H = 240 nm. Red arrows represent magnetic field vectors, and white arrows represent electric field vectors. **g** and **h** Transmission spectra at (P = 420 nm, R = 92 nm, and H = 300 nm) as a function of different incident angle for p- and s-polarized under azimuthal angle $\varphi = 0°$, respectively. **i** Transmission amplitudes and corresponding fits at 800 nm for p- and s-polarized in the case of oblique incidence, respectively

the cylinder are modulated to satisfy the desired requirements. Transmission spectra are calculated using finite difference time domain (FDTD) method. In order to obtain the expected electromagnetic response and resonance spectra, R = 90 nm is fixed. As shown in Fig. 2b, the transmission spectra are calculated for height H ranges from 100 to 400 nm in the normal incident. It is clear that the transmission spectrum is dominated by two resonance modes and both modes are controlled by the height of the cylinder. As the height of the cylinder increases, both resonant modes red-shifted and gradually approach each other. At H = 300 nm, the two resonance modes merges and a broadband approximately zero transmission region is obtained. When the height is further increased the transmission amplitude of the metasurface becomes non-zero. Therefore, the height of the cylinder is fixed to H = 300 nm.

To understand the physical mechanisms of the two resonance modes in Fig. 2b, we investigated the resonance characteristics of the metasurface at the wavelengths of 716 nm and 806 nm by using Finite element method when P = 420 nm, R = 90 nm, and H = 240 nm, as shown in Fig. 2c-f. As shown in Fig. 2c-d, at 716 nm resonant mode, two electric vector loops with opposite directions along the y-axis in the x–y plane of the metasurface, and induced magnetic field vectors to generate an anticlockwise direction magnetic vector loop in the y–z plane. Thus, an electric toroidal dipoles (ETD) resonance is formed with the polar moment direction along the x-axis positive direction. For the resonant mode around 806 nm the magnetic and electric field profiles are calculated as shown in Fig. 2e and f respectively. Figure 2e and f shows that the resonance in the case can lead to two magnetic vector loops in opposite directions in the x-axis direction of the metasurface in the x–y plane, and the consequent induced electric field vectors can generate an electric vector loop in the x–z plane in the anticlockwise direction. Thereby, a magnetic toroidal dipoles (MTD) resonance can be formed with the polar moment direction along the y-axis negative direction. Meanwhile, it can also find that the polar moment directions of the two toroidal dipoles (TD) resonances generated at 716 nm and 806 nm are orthogonal, in which case it can help to induce further detuning of such ETD and MTD resonances by modifying the geometrical parameters of the cylindrical metasurface, and thus contribute to the obtaining of a broadband region with zero transmission amplitude.

Next, we investigate the effect of R on the transmission spectra, where R is varied from 60 to 120 nm when the height of the cylindrical metasurface is set to H = 300 nm at P = 420 nm (for details, see Sect. 1, Supplementary Material). The spectral region with zero transmission is redshifted and broadened with increasing R. Considering that the chosen operating wavelength is in the proximity of 800 nm, R = 92 nm was finally chosen for the cylinder (for details, see Sect. 1, Supplementary Material). So, the region where the transmission amplitude of the designed metasurfaceis approximately zero can be limited to 50 nm within the range from775 nm to 825 nm. Such a zero-value transmission bandwidth is very difficult to realize for a single low Q-factor resonant metasurface. Additionally, due to the rotational symmetry of the designed cylindrical metasurface, the same result can be obtained by replacing the p-polarized with s-polarized incident beam (for details, see Sect. 1, Supplementary Material).

Transmission spectral analysis of metasurface

For the purpose of clearly understanding, the relationship between the transmission spectra of cylindrical metasurface under different polarization conditions and the incidence angle are presented. The transmission of p- and s-polarized are simulated as a function of wavelength and incidence angle for the range of the maximum oblique incidence angle θ_{max} up to 40° when the azimuthal angle $\varphi = 0°$are shown in Fig. 2g and h, respectively. It can be seen that in the wavelength range from 780 to 840 nm, the transmission amplitudes vary with the increase of the oblique incidence angle in the two orthogonal polarization states. At normal incidence, the transmission spectra and resonance positions of p- and s-polarization are identical in the range of 780 nm to 840 nm because of the C_6 rotational symmetry satisfied by the metasurface unit cell. However, the transmission spectra change significantly when the incidence is oblique. For p-polarized, from the transmission spectra in Fig. 2g, it can be found that along with the increase of the incidence angle from 0° to 40°, the resonance modes near 780 nm and near 840 nm undergo a slight blue-shift and red-shift, respectively. This leads to broaden the spectrum and the transmission amplitude is gradually increasing. For the s-polarized, it can be shown from the transmission spectra in Fig. 2h that the resonance modes near 780 nm and those near 840 nm remain essentially unchanged when the incident angle increase from 0° to 40°. However, in the detuning range between them, the bound states in the continuum (BIC) present in the transmission spectrum are observed as the oblique incidence angle increases, leading to the excitation of the BICs towards quasi-BIC (Q-BIC) with a sufficiently observable high Q-factors (for details, see Sect. 2, Supplementary Material). Meanwhile, these Q-BIC resonance modes exhibit a slight redshifted when the incident angle increases, accompanied by a gradual increase in the transmission amplitude at the corresponding wavelengths.

Additionally, we fit the transmission spectra of p- and s-polarized light as a function of the oblique incidence angles for the case of 800 nm, respectively, as shown in Fig. 2i. It is can find that the transmission amplitude and oblique incidence angle of the metasurface satisfy the quadratic relationship in these two orthogonal polarization states, which provide the necessary conditions for the dual-polarization channel to realize the Laplace operation. Moreover, such dual polarization channels are in the same wavelength range, which is different from most of the current differentiators operating in individually polarized channels. Moreover, from Fig. 2i, it can be observed that the maximum fitting value of the quadratic curve can reach $NA(\sin(\theta)) \approx 0.64$, which indicates the edge detection resolution $(0.61 \cdot \lambda/NA)$ of this Laplace differentiator can reach 0.7625 μm. Although the transmission efficiency is low in s-polarization channel, it does not affect the implementation of the Laplace differentiation operation with large NA. Moreover, the transmission amplitude of p-polarization reaches 0.93 at the maximum incidence angle 40°, this ensures that the maximum operating efficiency can reach up to 86.49%. So, for this design of the cylindrical metasurface has the potential to achieve image edge detection with dual polarization channels, large NA and high resolution.

Broadband isotropy optical transfer function analysis of metasurface

According to the definition of the Laplace differential operator, it is also required that the angle-dependent optical transfer function satisfies the independence of different

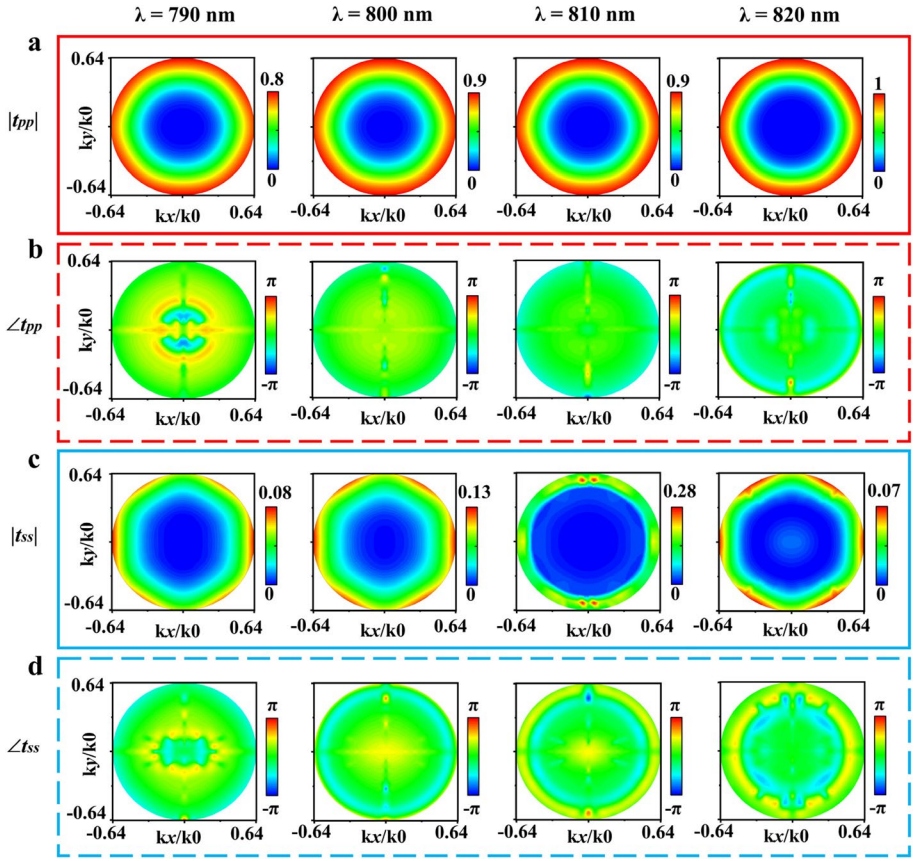

Fig. 3 Two-dimensional dispersive behaviors of the cylindrical metasurface for p- and s-polarized incidence at different wavelengths range from 790 to 820 nm. **a** and **c** are the angularly distributed transmittance amplitude of the metasurface for p- and s-polarized conditions for incidence within 0° to 40° (corresponding to $k_x/k_0 = \pm 0.64$), respectively. **b** and **d** are the angularly distributed transmittance phase of the metasurface for p- and s-polarized conditions for incidence within 0° to 40° (corresponding to $k_x/k_0 = \pm 0.64$), respectively

azimuthal angles. For this reason, the transmission spectra and phases of incident light of four different wavelengths were simulated for different azimuthal angles in p- and s-polarized light for arbitrary wave vectors, as shown in Fig. 3. During the simulation, the incident light of different polarization states with the incident angle θ is set from 0° to 40° in 5° steps, and the azimuth angle φ is also set in 5° steps from 0° to 360°.

Based on the fact that the two-dimensional transmission angular dispersion spectra of the cylindrical metasurface at four different wavelength positions, 790 nm, 800 nm, 810 nm, and 820 nm, exhibit nearly isotropic profiles for both p- and s-polarized polarizations in Fig. 3a and c, respectively. Namely, the cylindrical metasurfaces within the maximum incidence angle range are not sensitive to the azimuthal angle. This is good evidences that such a metasurface can maintain good two-dimensional isotropic or azimuth-independent properties for the transmission spectra at any incidence angle within the range of the maximum incidence angle. Meanwhile, the transmission phase distributions are calculated for four wavelengths as shown in Fig. 3b and d, respectively. It is shown that the cylindrical metasurface provides similar phases for arbitrary in-plane wave vector for p- and s-polarization with regard to arbitrary azimuthal angle within the

designed incidence angle range. Therefore, the optical transfer function of such a metasurface at p- and s-polarization satisfies the definition of Laplace operation.

Next, we further investigate the broadband properties of the Laplace differentiator of the designed cylindrical metasurface in p- and s-polarized conditions. Extra analysis is carried out for different wavelengths in the range of 780 nm to 840 nm, which also allowes the realization of the Laplace differentiation operation (for details, see Sect. 3 and Sect. 4, Supplementary Material). In addition, the metasurface differentiator designed in this work also has the potential to perform in unpolarized light in the range of 780 nm to 840 nm, which is expected to be better integrated into conventional imaging systems.

Imaging results of the designed Laplace differentiator

Sample processing and spectral test

To experimentally verify the effectiveness and image processing capability of the designed metasurface, a 900 μm × 900 μm metasurface differentiator is fabricated by electron beam lithography (EBL) and reactive ion etching process. The top and side views of its scanning electron microscope (SEM) images are shown in Fig. 4a and b, respectively, which shows a good performance of fabrication. Next, the transmission of metasurface is measured with custom-built setup, as shown in Fig. 4c. A standard microscopy path is applied, where the supercontinuum laser (NKT Photonics Superk EVO) is used for light source, and a spectrometer is used to detect the transmittance of metasurface. By rotating the polarizer and translation stage, the transmission spectra of the metasurface can be obtained in different polarization and incident angles.

The oblique incidence spectra at different polarizations were measured using the setup with the azimuthal angle at zero. Figure 4d and f are the simulation spectra at incidence of p- and s-polarized light extracted from Fig. 2g and h, respectively. As shown in Fig. 4e, for the measured spectra of the p-polarized, when the incident angle is varied from normal incident to the oblique incident angle, it can be found that the measured spectra in the waveband of 750 nm to 850 nm can be well matched with the simulation. Note there is a slight blueshift in the metasurface transmission spectrum due to a small inaccuracy in the fabrication, it in contrast produces a little broader broadband effect for the actual differentiation. After rotating the polarizer at 90°, the measured s-polarized spectra for different angles are shown in Fig. 4g. Compared to the simulated spectra in Fig. 4f, the experimental spectra also show a certain degree of blueshift. Since the tip of the Q-BIC spectrum is too narrow beyond the resolution of the spectrometer it cannot be fully fitted, but this does not affect the differential effect of the metasurface. Thus, based on the SEM images and spectroscopic measurements, it is clear that the fabricated sample can fulfill the desired design.

Experimental results of edge detection

Next, we demonstrate the image edge detection functionality of the fabricated metasurface samples. The new experimental setup is shown in Fig. 5a, which from left to right consists of the laser source, test target, metasurface differentiator, and an amplification system composed of the microscope objective (50x/0.65), a tubular lens, and a near-infrared camera for imaging the test target. Among them, the Optical Parametric

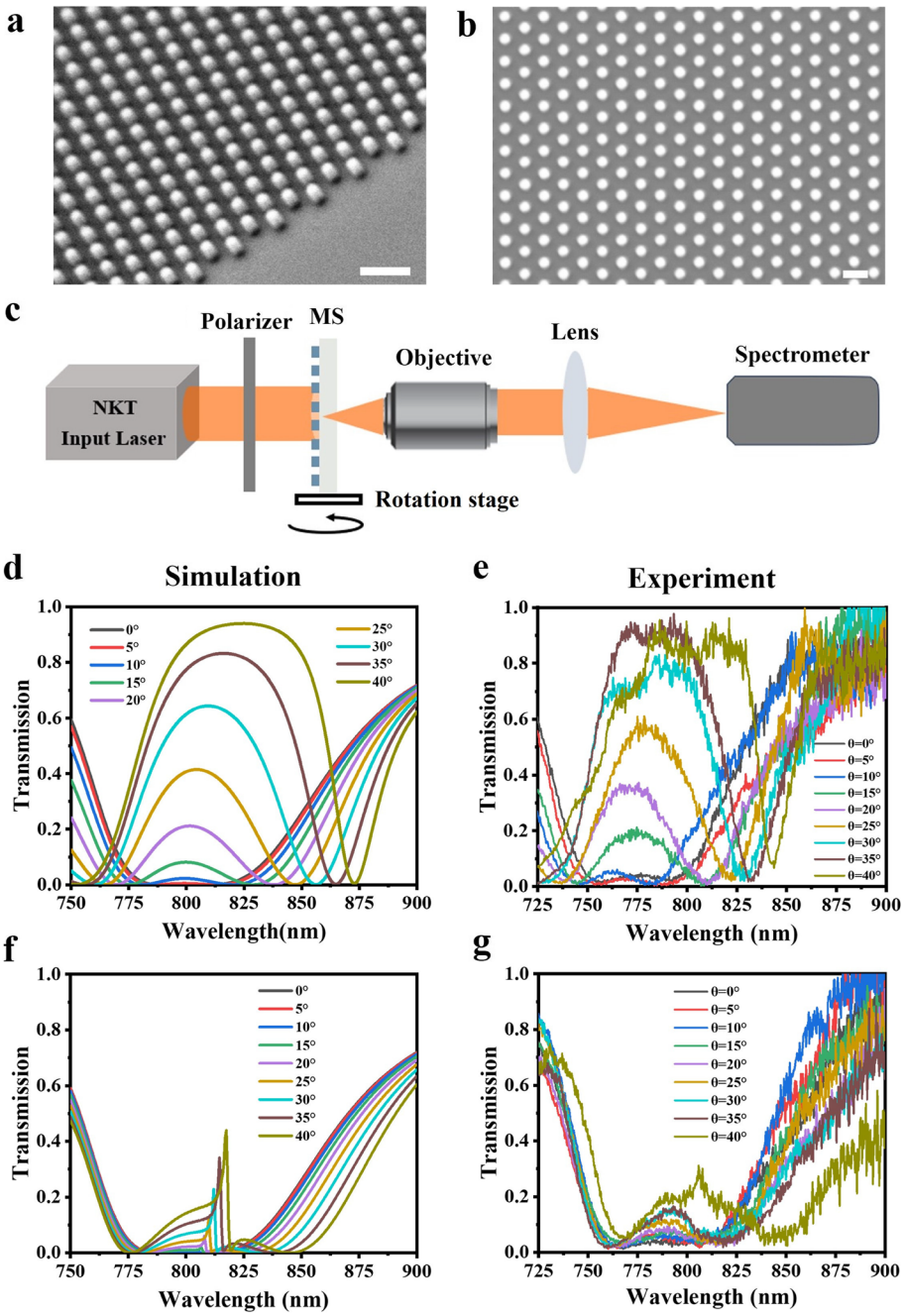

Fig. 4 Fabrication and characterization of the metasurface. **a** and **b** SEM images in top and side views of the fabrication metasurface sample with scale bars of 1 μm and 500 nm, respectively. **c** Experimental setup for metasurface spectral measurement. A polarizer is used to control the polarization of the incident beam. The lens images the back focal plane of the objective (40 × /0.6) to the spectrometer. **d** and **e** Simulated and experimental spectra under p-polarized, respectively. **f** and **g** Simulated and experimental spectra under s-polarized light, respectively

Oscillator (OPO) provides a nanometer-tunable incident light source with polarization characteristics. In the experiment, we placed the metasurface differentiator at an appropriate distance behind the target so that the differentiator can better filter the incident wave vectors in different directions of the target image. The polarization direction of the

incident beam can be modified simply by adding a half waveplate in front of the detection target of the experimental setup shown in Fig. 5a.

To begin with, the alphabets "BIT" and "META" with irregular edges were used as input images for the p- and s-polarized illumination at a wavelength of 800 nm, as shown in Fig. 5b and e, respectively. The average width of each letter is about 100 μm. When the metasurface differentiator is added into the experimental process, the edge detection results can be quickly observed as shown in Fig. 5c and f, respectively. Obviously, the edge information of all the alphabets can be clearly captured. By experimentally measuring and comparing the normalized intensity distributions at the horizontal cut line positions in Fig. 5b and c under p-polarized illumination, it can be clearly seen in Fig. 5d that with two closely peaks formed around each edge of the target image. The same phenomenon can also be observed by comparing the normalized intensity distributions at the vertical cut line positions in Fig. 5e and f under s-polarized illumination, and the results are shown in Fig. 5g. This sufficiently demonstrates the ability of our designed cylindrical metasurface Laplace differentiator can directly achieve second-order two-dimensional edge detection in the spatial space with dual polarization channels for target objects without 4f system. Meanwhile, for edge detection of straight lines (the input image was taken from the 1951 USAF resolution test chart using Group 4, Element 1, and the corresponding numbers from "1" to "6") and circular curves (the input image was coming from a circular mask pattern fabricated by direct laser writing) show good edge detection results in each polarization channel (for details, see Sect. 5, Supplementary Material).

Furthermore, the actual resolution of the differentiator device is an important and significant performance metric that directly determines the imaging performance. The theoretical analysis section has predicted that this designed metasurface Laplace differentiator can achieve an edge detection resolution up to 0.7625 μm due to the achievable large NA performance close to the 0.64. However, this exceeds the minimum size of common standard resolution plates. For this, a set of 12 samples with a length of 500 μm and a width increasing sequentially from 0.5 μm to 1.0 μm and 1.2 μm to 2.2 μm were fabricated using photoresist material by the home group's processing equipment, as shown in Fig. 5h. These sample patterns at this moment are obtained under illumination with 800 nm p-polarized light without the metasurface differentiator. The observed result directly under white light source is detailed in Sect. 6 of the Supplementary Material. After adding the metaurface differentiator, the edge detection effect is shown in Fig. 5i, essentially reaching the theoretical resolution. By comparing the normalized intensity distributions at the vertical cut positions of the third group (width: 0.7 μm) and the fourth group (width: 0.8 μm) samples

(See figure on next page.)

Fig. 5 Edge detection test of the metasurface differentiator under 800 nm. **a** Schematic of the experimental setup for edge detection. **b**-**c** and **e**–**f** Results of imaging about the alphabet letters "BIT" and "META" without and with the metasurface differentiator in the case of p- and s-polarized, respectively. Scale bars: 100 μm. **d** and **g** Normalized intensity contrasts corresponding to the horizontal and vertical cut line positions in (b)-(c) and (e)-(f), respectively. **h-i** Imaging results of custom lithography samples without and with the matasurface differentiator, respectively. **j** Normalized intensity contrasts corresponding to the vertical cut line positions in (h) and (i), respectively

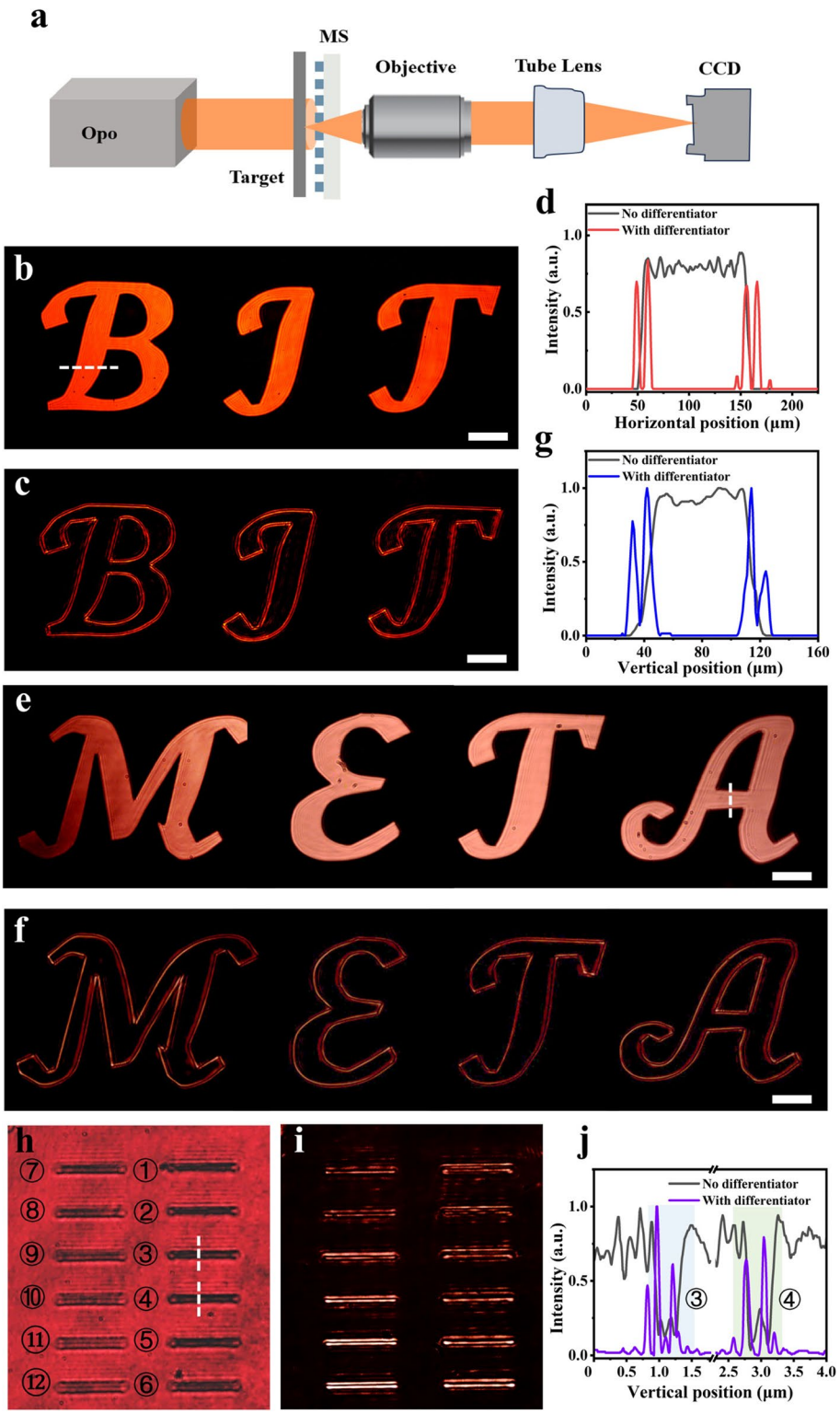

Fig. 5 (See legend on previous page.)

under p-polarized illumination in Fig. 5h and i, the edge features of the stripe patterns can be clearly observed, and the results are shown in Fig. 5j. Similarly, adjusting the incident light to s-polarization also yields analogous experimental results (for details, see Sect. 6, Supplementary Material). It is shown that such a differentiator can realize better resolution, which can be important for image processing applications of small details.

Broadband coherent edge detection experiments

For the analysis of the broadband isotropic performance of the metasurface differentiator, it is demonstrated that the metasurface differentiator can realize broadband Laplace differentiation operations at both p- and s-polarization. Then, onion epidermal cells are utilized for the corresponding verification. Firstly, without the metasurface differentiator in the experimental setup, the imaging of onion epidermal cells under the illumination

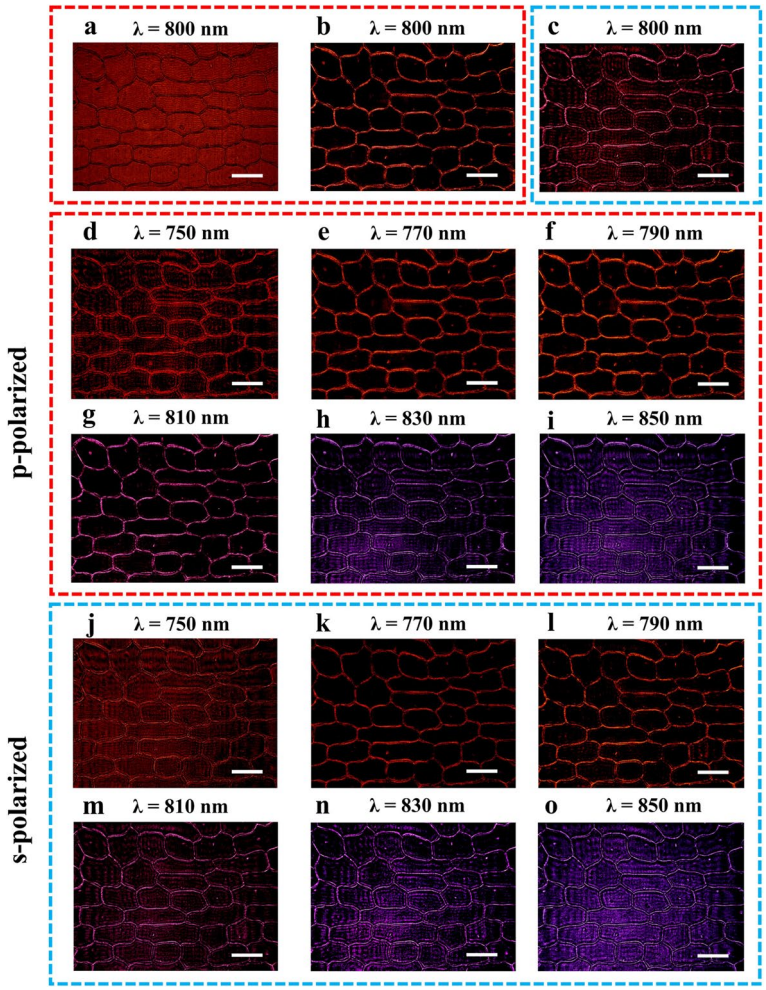

Fig. 6 Dual-polarized broadband edge detection for onion epidermal cells with metasurface differentiator. **a** Imaging of onion epidermal cells without metasurface differentiator. **b**-**c** Edge detection imaging of onion epidermal cells under p- and s-polarized light at 800 nm with metasurface differentiator. **d**-**i** and **j**-**o** Edge detection results under p- and s-polarized at different wavelengths in 750- 850 nm waveband, respectively. Scale bars: 50 μm

of 800 nm are shown in Fig. 6a, where the boundaries of neighboring onion epidermal cells are indistinguishable. As the metasurface differentiator was added, all the edges and contours of the onion epidermal cells can be clearly recognized under both p- and s-polarization, as shown in Fig. 6b and c, respectively. Afterwards, the broadband edge detection test was carried out. Because of the blue shift occurred in the spectrum of the actual fabricated metasurface differentiator, the Laplace differentiation can be performed in a wider spectrum. Therefore, broadband edge detection of onion epidermal cells was performed from 750 nm up to 850 nm at p- and s-polarized illumination. The corresponding results are shown in the red boxes in Fig. 6d-i and j-o, respectively.

Compare with the edge detection results at the corresponding wavelengths under s-polarized depicted in Fig. 6j-o, it can be discovered that the edge detection at p-polarized is clearly. This is mainly attributed to the fact that the intensity of p-polarized transmission increases with the angle of oblique incidence to a higher extent than that of s-polarized. However, broadband second-order two-dimensional edge detection for the onion epidermal cells can be achieved in both polarization states. As a result, cells such as transparent onion epidermis can be easily identified in the range of 750 nm to 850 nm, which facilitates the observation of cell morphology and behavioral in biological research. Simultaneously, such metasurface differentiator can provide a larger NA range as well as higher spatial resolution conveniently in the image edge detection within dual polarization channels.

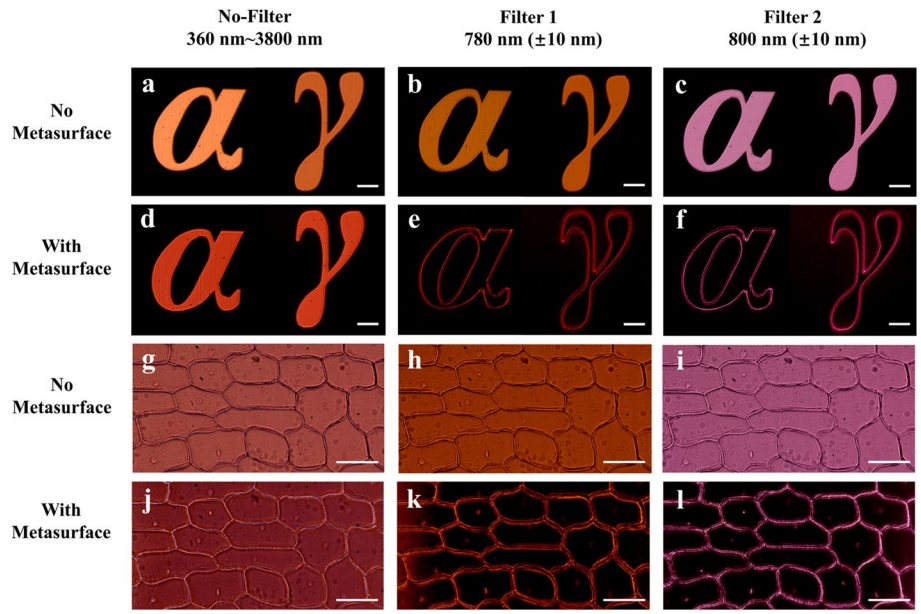

Fig. 7 Edge detection of the metasurface differentiator under the illumination of incoherent and unpolarized sources. **a**-**c** Results of direct imaging of fabricated alphabet samples without filter, and with filters centered at 780 nm and 800 nm with a full width at half maximum (FWHM) of 10 nm, when no metaurface differentiator is placed in the experimental setup, respectively. Scale bars: 100 μm. **d**-**f** Corresponding to the imaging results after adding the metasurface differentiator in to the experiment in (**a**)-(**c**). **g**-**i** and **j**-**l** Experimental procedure was the same as (**a**)-(**c**) and (**d**)-(**f**), respectively, just that the test target was changed to onion epidermal cells. Scale bars: 50 μm

Broadband incoherent edge detection experiments

Considering that in practical real-life scenarios, incoherent light is more common than coherent source. To verify the response of the designed Laplace metasurface differentiator under incoherent condition, we use tungsten halogen light source to replace the laser source illuminate the target object, which can provide a continuous, stable, unpolarized and uniform broadband incoherent light in 360–3800 nm waveband. Test patterns were made with alphabetic masks fabricated in home group and onion epidermal cells. For the alphabetic pattern, the bright field imaging results are shown in Fig. 7a. However, when metasurface differentiator is added that the expected edge detection results still could not be obtained, as shown in Fig. 7d. This is mainly attributed to the fact that the tungsten halogen light source can provide continuous spectrum from 360 to 3800 nm, which causes the imaging range to not only include but also exceed the operating wavelength range for which the metasurface differentiator can perform, edge detection. In this case, the bright field imaging beyond the operating wavelength part of the metasurface differentiator is mixed with the edge detection imaging results, which ultimately leads to the inability to observe the differentiation results of the target image to be observed. It is necessary to place a suitable filter behind the tungsten halogen light source, so as to intercept the range of wavelengths where the metasurface differentiator can work properly. When the filters with center wavelengths of 780 nm and 800 nm and full width at half maxima (FWHM) of ± 10 nm are placed behind the incident source of the experimental setup, the imaging results without the metasurface differentiator are shown in Fig. 7b and c. At this moment, when the metasurface differentiator is added, the second order two-dimensional image edge detection results can be generated directly, as shown in Fig. 7e and f. It is important to highlight that it is different from the broadband edge detection at different wavelengths for a single wavelength in Fig. 6. The edge detection in Fig. 7e and f results in a single imaging shot to obtain second-order two-dimensional edge detection under incoherent light and unpolarized conditions in a broadband region of 20 nm or wider, which is of great value in practical applications.

Utilizing the same measurement method, the alphabetical pattern in the experiment was replaced with onion epidermal cells. In the absence of the metasurface differentiator or only adding the filter, the bright-field imaging is shown in Figs. 7g-i. While, when inserting the metasurface differentiator and the filters with center wavelengths of 780 nm and 800 nm and FWHM of ± 10 nm, it also obtains clear incoherent, unpolarized, and broadband second-order two-dimensional edge-detection images of the onion epidermal cells, as shown in Figs. 7k-l. This direct implementation of broadband Laplace differential operations and image second-order two-dimensional edge detection in incoherent and unpolarized light illumination conditions without relying on a the 4f system is significant in compact image processing applications.

Conclusion

In conclusion, we have theoretically proposed and experimentally demonstrated an approach to design a single-layer metasurface Laplace differentiator composed of hexagonal lattice periodic cylindrical for all-optical computing and isotropic image edge detection, while simultaneously maintaining large broadband, high-NA, and excellent isotropy, even with incoherent and unpolarized illumination. The metasurface Laplace

differentiator can obtain a large operating bandwidth with zero transmittance in the near-infrared region by supporting the detuning of ETD and MTD resonance modes at normal incident. In this broadband range, the transmission amplitudes under the p- and s-polarized channels satisfy the relationship of quadratic function with the increase of oblique incidence angle, for their optical transfer functions to fulfill the Laplace differential operator in real space under the dual-polarized channels, respectively. Numerical calculations and experimental results of this metasurface differentiator are performed in good agreement. The NA and experimental resolution can reach 0.64 and 0.7625 μm, respectively. Meanwhile, Laplace differentiation operation and second-order two-dimensional image edge detection can be realized in the wavelength range close to 100 nm for coherent and incoherent, polarized and unpolarized, as well as multi-wavelength narrowband and broadband illumination conditions. Thanks to the metasurface Laplace differentiator does not require a conventional 4f filtering system, it is also suitable for direct integration into existing commercial imaging applications, providing a viable platform for realizing more compact, ultra-low-power, ultra-fast all-optical data and image processing systems. Furthermore, leveraging advanced strategies such as neural networks or inverse design to explore more powerful metasurface is beneficial for applying optical differentiation and image edge detection techniques to practical complex conditions and highly integrated commercial optical systems. For instance, the application of optical differentiation technology can be extended to quantitative phase imaging [42, 43], spatiotemporal information modulation [44, 45], and even multifunctional dynamic display imaging [22, 38, 46], providing a solid application platform for the advancement of more sophisticated image processing in the future.

Methods

Simulations

The transmission spectra in Fig. 2b and g-h were calculated using the commercial FDTD Lumerical software. For the unit cell simulation, the plane wave sources came from the substrate side and with the propagation direction of + z was placed inside the SiO2 substrate. The periodic boundary conditions (PBC) were used along x and y axes. Meanwhile, perfectly matched layers (PMLs) were added at the top and bottom as the boundaries along z axis. The transmitted fields were recorded from a field monitor that is placed above the structures. The electromagnetic profiles in Fig. 2c-f were simulated using commercial software COMSOL Multiphysics. PMLs were added at the top and bottom of the structure. PBC were applied in the x and y directions to simulate the periodic unit cell. The refractive index of silica substrate is 1.45.

Sample fabrication

Our proposed Laplace differentiator metasurface was fabricated on a fused quartz substrate by utilizing electron beam lithography (EBL) and reactive ion etching (RIE). Firstly, a 300-nm-thick amorphous silicon (α-Si) film was deposited by plasma enhanced chemical vapor deposition (PECVD) method. Then, a PMMA electron beam resist (EBR) of 200 nm was spinning coated onto Si substrate. The desired structure was patterned by utilizing JEOL 6300FS EBL at a base dose of 1000 μC/cm2 with an accelerating voltage of 100 kV. After the exposure process, the resist was developed in 1:3 MIBK:IPA solution

for 40 s and rinsed in IPA for 30 s successively, followed by a deposition of 80 nm Cr using electron beam evaporation deposition (EBD) method. For the purpose of realizing the lift-off process, the sample was immersed in hot acetone of 65℃ and cleaned by ultrasonic. Finally, by using inductively coupled plasma reactive ion etching (RIE) method with HBr at room temperature (RT) for 180 s (flow rate of 50 sccm, pressure of 10 mTorr, RF and ICP power of 50 and 750 W, respectively), the desired structure was transferred from Cr to silicon and the remaining Cr was removed by cerium (IV) ammonium nitrate. For visualizing the fabrication process of the metasurface, we provide a schematic to show the fabrication processes of the metasurface step by step (for details, see Sect. 7, Supplementary Material).

Abbreviations

NA	numerical aperture
TD	toroidal dipole
ETD	electric toroidal dipole
MTD	magnetic toroidal dipole
AR	augmented reality
VR	virtual reality
OTF	optical transfer function
FDTD	finite difference time domain
BIC	the bound states in the continuum
Q-BIC	quasi - bound states in the continuum
CCD	Charge - coupled Device
EBL	electron beam lithography
RIE	reactive ion etching
PECVD	plasma enhanced chemical vapor deposition
EBR	electron beam resist
EBD	evaporation deposition
RT	room temperature

Supplementary Information

The online version contains supplementary material available at https://doi.org/10.1186/s43074-025-00168-5.

Additional file 1.

Acknowledgements
L.L. Huang acknowledges technical support from the Laboratory of Microfabrication, Institute of Physics, CAS for sample fabrication.

Authors' contributions
L.H., Y.W., and C.Z. proposed the idea. L.H. and C.Z. conducted pattern designs and numerical simulations. G.G., J.L. and X.L. fabricated the samples. L.H., R.Z., Y.C, and C.Z. performed the experimental measurements. L.H., N.M., Y.W., and C.Z. prepared the manuscript. L.H., Y.W., and X.L. supervised the overall projects. All the authors analyzed the data and discussed the results.

Funding
The authors acknowledge funding provided by the National Key R&D Program of China (2021YFA1401200), the National Natural Science Foundation of China program (No. U21A20140), the National Science Fund for Distinguished Young Scholars (No. 52325505), and the Beijing Natural Science Foundation (JQ24028).

Data availability
The datasets used and/or analyzed during the current study are available from the corresponding author on reasonable request.

Declarations

Ethics approval and consent to participate
All authors participate in this work and manuscript.

Consent for publication
All authors agreed to publish this paper.

Competing interests
The authors declare no conflicts of interest.

Received: 26 December 2024 Revised: 14 March 2025 Accepted: 18 March 2025
Published online: 03 April 2025

References

1. Wang C, Mei X, Pan L, Wang P, Li W, Gao X, Bo Z, Chen M, Gong W, Han S. Airborne near infrared three-dimensional ghost imaging LiDAR via sparsity constraint. Remote Sensing. 2018;10(5):732.
2. Tittl A, Leitis A, Liu M, Yesilkoy F, Choi DY, Kivshar YS, Altug H. Imaging-based molecular barcoding with pixelated dielectric metasurfaces. Science. 2018;360(6393):1105–9.
3. Kim Y, Lee GY, Sung J, Jang J, Lee B. Spiral Metalens for Phase Contrast Imaging. Adv Funct Mater. 2021;32(5):2106050.
4. Gopakumar M, Lee GY, Choi S, Chao B, Peng Y, Kim J, Wetzstein G. Full-colour 3D holographic augmented-reality displays with metasurface waveguides. Nature. 2024;629(8013):791–7.
5. Ambs P. Optical computing: a 60-year adventure. Adv Opt Technol. 2010;2010:1–15.
6. Solli DR, Jalali B. Analog optical computing. Nat Photonics. 2015;9:704–6.
7. Wang Z, Li T, Soman A, Mao D, Kananen T, Gu T. On-chip wavefront shaping with dielectric metasurface. Nat Commun. 2019;10:3547.
8. Roberts A, Gómez DE, Davis TJ. Optical image processing with metasurface dark modes. J Opt Soc Am A. 2018;35(9):1575–84.
9. Tang P, Kim Y, Badloe T, Xiao LL, Yang YG, Kim M, Rho J, Li GQ. Polarization-independent edge detection based on the spin–orbit interaction of light. Opt Express. 2024;32(10):17560.
10. Tang P, Li XT, Kim Y, Xiao LL, Wu HP, Badloe T, Li GQ, Rho J. Spin hall effect of light in a dichroic polarizer for multifunctional edge detection. ACS Photonic. 2024;11(10):4170–6.
11. Li Y, Chen S, Liang H, Ren X, Luo L, Ling Y, Liu S, Su Y, Wu ST. Ultracompact multifunctional metalens visor for augmented reality displays. PhotoniX. 2022;3(1):29.
12. Chen WT, Zhu AY, Capasso F. Flat optics with dispersion-engineered metasurfaces. Nat Rev Mater. 2020;5(8):604–20.
13. Estakhri NM, Edwards B, Engheta N. Inverse-designed metastructures that solve equations. Science. 2019;363(6433):1333–8.
14. Chen C, Qi W, Yu Y, Zhang X. On-chip optical spatial-domain integrator based on Fourier optics and metasurface. Nanophotonics. 2021;10(9):2481–6.
15. Fu W, Zhao D, Li Z, Liu S, Tian C, Huang K. Ultracompact meta-imagers for arbitrary all-optical convolution. Light Sci Appl. 2022;11(1):62.
16. Silva A, Monticone F, Castaldi G, Galdi V, Alù A, Engheta N. Performing mathematical operations with metamaterials. Science. 2014;343(6167):160–3.
17. Abdollahramezaniy S, Hemmatyary O, Adibi A. Meta-optics for spatial optical analog computing. Nanophotonics. 2020;9(13):4075–95.
18. Guo C, Xiao M, Minkov M, Shi Y, Fan SH. Photonic crystal slab Laplace operator for image differentiation. Optica. 2018;5(3):251–6.
19. Abdollahramezani S, Chizari A, Dorche AE, Jamali MV, Salehi JA. Dielectric metasurfaces solve differential and integro-differential equations. Optics Letters. 2017;42:42 (7).
20. Zhou J, Qian H, Chen CF, Zhao J, Li G, Wu Q, Luo HL, Wen SC, Liu ZW. Optical edge detection based on high-efficiency dielectric metasurface. Proc Natl Acad Sci. 2019;116(23):11137–40.
21. Huo P, Zhang C, Zhu W, Liu M, Zhang S, Zhang S, Chen L, Lezec HJ, Agrawal A, Lu Y. Photonic spin-multiplexing metasurface for switchable spiral phase contrast imaging. Nano Lett. 2020;20(4):2791–8.
22. Liang X, Zhou Z, Li Z, Li J, Peng C, Cui H, Wei K, He Z, Yu S, Zheng G. All-Optical Multiplexed Meta-Differentiator for Tri-Mode Surface Morphology Observation. Adv Mater. 2023;35(29):2301505.
23. Goodman J. Introduction to Fourier optics. 2rd Edition. Englewood: Roberts and Company Publishers; 1995.
24. Zhu T, Zhou Y, Lou Y, Ye H, Qiu M, Ruan Z, Fan SH. Plasmonic computing of spatial differentiation. Nat Commun. 2017;8:15391.
25. Dong Z, Si J, Yu X, Deng X. Optical spatial differentiator based on subwavelength high-contrast gratings. Appl Physics Letters. 2018;112:112 (18).
26. Zhou Y, Zheng H, Kravchenko II, Valentine J. Flat optics for image differentiation. Nat Photonics. 2020;14(5):316–23.
27. Jin C, Yang Y. Transmissive nonlocal multilayer thin film optical filter for image differentiation. Nanophotonics. 2021;10(13):3519–25.
28. Pors A, Nielsen MG, Bozhevolnyi SI. Analog computing using reflective plasmonic metasurfaces. Nano Lett. 2014;15(1):791–7.
29. Cordaro A, Kwon H, Sounas D, Koenderink AF, Alù A, Polman A. High-index dielectric metasurfaces performing mathematical operations. Nano Lett. 2019;19(12):8418–23.
30. Dai C, Li Z, Shi Y, Wan S, Hu W, Li Z. Hydrogel-Scalable Nanoslide for Switchable Optical Spatial-Frequency Processing. Laser Photonics Rev. 2023;17(4):2200368.
31. Kwon H, Cordaro A, Sounas D, Polman A, Alù A. Dual-polarization analog 2D image processing with nonlocal metasurfaces. ACS Photonics. 2020;7(7):1799–805.
32. Zhou J, Qian H, Zhao J, Tang M, Wu Q, Lei M, Luo H, Wen S, Chen S, Liu Z. Two-dimensional optical spatial differentiation and high-contrast imaging. Natl Sci Rev. 2021;8(6):nwaa176.
33. Pan D, Wan L, Ouyang M, Zhang W, Potapov AA, Liu W, Liang Z, Feng T, Li Z. Laplace metasurfaces for optical analog computing based on quasi-bound states in the continuum. Photonics Res. 2021;9(9):1758–66.

34. Zhou Y, Wu W, Chen R, Chen W, Chen R, Ma YG. Analog optical spatial differentiators based on dielectric metasurfaces. Adv Opt Mater. 2019;8(4):1901523.
35. Komar A, Aoni RA, Xu L, Rahmani M, Miroshnichenko AE, Neshev DN. Edge detection with mie-resonant dielectric metasurfaces. ACS Photonics. 2021;8(3):864–71.
36. Cotrufo M, Arora A, Singh S, Alù A. Dispersion engineered metasurfaces for broadband, high-NA, high-efficiency, dual-polarization analog image processing. Nat Commun. 2023;14:7078.
37. Wang H, Guo C, Zhao Z, Fan SH. Compact incoherent image differentiation with nanophotonic structures. ACS Photonics. 2020;7(2):338–43.
38. Zhang XM, Bai BF, Sun HB, Jin G, Valentine J. Incoherent optoelectronic differentiation based on optimized multilayer films. Laser Photonics Rev. 2022;16(9):2200038.
39. Tanriover I, Dereshgi SA, Aydin K. Metasurface enabled broadband all optical edge detection in visible frequencies. Nat Commun. 2023;14:6484.
40. Bracewell R. The Fourier Transform and Its Applications. 3rd Edition. McGraw Hill; 2000.
41. Suh W, Wang Z, Fan SH. Temporal coupled-mode theory and the presence of non-orthogonal modes in lossless multimode cavities. IEEE J Quantum Electron. 2004;40(10):1511–8.
42. Wesemann L, Rickett J, Song J, et al. Nanophotonics enhanced coverslip for phase imaging in biology. Light Sci Appl. 2021;10(90):2047–7538.
43. Ji A, Song JH, Li Q, et al. Quantitative phase contrast imaging with a nonlocal angle-selective metasurface. Nat Commun. 2024;13(1):7848.
44. Esfahani S, Cotrufo M, Alù A, et al. Tailoring space-time nonlocality for event-based image processing metasurfaces. Phys Rev Lett. 2024;133(6): 063801.
45. Cotrufo M, Esfahani S, Korobkin D, et al. Temporal signal processing with nonlocal optical metasurfaces. NPJ Nanophotonics. 2024;1(1):39.
46. Badloe T, Kim Y, Kim J, et al. Bright-field and edge-enhanced imaging using an electrically tunable dual-mode metalens. ACS Nano. 2023;17(15):14678–85.

Publisher's Note